Top Catal (2016) 59:292–302
DOI 10.1007/s11244-015-0443-4

ORIGINAL PAPER

Steam Reforming of Toluene Over $Pt/Ce_xZr_{1-x}O_2/Al_2O_3$ Catalysts

T. P. de Castro[1,2] · R. P. S. Peguin[2,3] · R. C. R. Neto[2] · L. E. P. Borges[1] · F. B. Noronha[1,2]

Published online: 6 August 2015

Abstract Steam reforming of toluene was investigated over $Pt/Ce_xZr_{1-x}O_2/Al_2O_3$ catalysts with different ceria and zirconia content ($x = 0.25$, 0.50, 0.75, and 1.00). Toluene was used as model molecule representative of tar produced in biomass gasification. The main reactions over $Pt/Ce_xZr_{1-x}O_2/Al_2O_3$ catalysts are the steam reforming of toluene and the water–gas shift. The dealkylation of toluene to benzene and methane takes place only at the beginning of the reaction. Toluene conversion significantly decreases during the reaction for all catalysts excepted for $Pt/CeO_2/Al_2O_3$ catalyst. Catalyst deactivation was attributed to carbon deposition as revealed by Raman spectroscopy. A clear relationship is observed between the acidity of the catalyst and the amount of carbon formed over $Pt/Ce_xZr_{1-x}O_2/Al_2O_3$ catalysts. Decreasing the Ce/Zr ratio increased the density of acid sites as well as the amount of carbon formed. This result suggests that the main route for carbon deposition proceeds by the oligomerization of toluene molecule on the acid sites of the support. $Pt/CeO_2/Al_2O_3$ catalyst was quite stable during steam reforming of toluene without carbon deposition. For this catalyst, ceria covered the acid sites of alumina and did not introduce significant Lewis acid sites.

✉ F. B. Noronha
fabio.bellot@int.gov.br

[1] Chemical Engineering Department, Military Institute of Engineering, Praça Gal. Tiburcio 80, Rio de Janeiro 22290-270, Brazil

[2] Catalysis Division, National Institute of Technology, Av. Venezuela 82, Rio de Janeiro 20081-312, Brazil

[3] Present Address: Innovation and Technology – Catalysis, Braskem S.A., Via Oeste Lote 5, Triunfo, RS 95853-000, Brazil

Keywords Steam reforming of toluene · Gasification · Biomass · Hydrogen production · Pt catalysts

1 Introduction

Most of the world's energy production is currently based on fossil fuels like oil, coal and natural gas. However the use of non-renewable resources has led to a significant increase in CO_2 emissions, which are known to enhance the greenhouse effect. Thus, the reduction of such environmental impact has driven the search for renewable sources of energy, including biomass. The gasification of biomass has been seen as a promising technology to produce synthesis gas (H_2 and CO), which can be converted to liquid fuels [1]. However, clogging of the lines and heat exchangers, and coke formation on catalyst surface, due to high tar content in the product gas, have limited the use of biomass gasification in industrial processes [2].

The catalytic reforming process is a very attractive approach for tar removal. However, due to the complexity of tar composition, different model molecules representatives of tar have been used in the studies such as benzene, toluene, naphthalene and methylnaphthalene. Nickel-based catalysts have been extensively investigated for the steam reforming (SR) of toluene due to the high activity of Ni for C–C bond breaking and its low cost [3–17]. However, nickel catalysts undergo significant deactivation during steam reforming of toluene, mainly attributed to carbon deposition. Therefore, the design of a more coke-resistant, and thus stable catalyst for this reaction is currently still a challenge.

Particle size control and chemical modification of the catalyst have been commonly proposed as approaches to either hinder carbon formation or promote coke removal

from the catalyst surface. The metal particle size significantly influences the carbon deposition rate for steam reforming of hydrocarbons. The formation of carbon is reduced or inhibited on smaller Ni crystallite size [18, 19] by controlling the number of atoms in an ensemble. Mixed oxides such as perovskite- or hydrotalcites-type oxides have been reported as promising catalyst precursors for SR of toluene [10–16]. The reduction of these mixed oxides result in thermally stable and highly dispersed metallic particles. In addition, the perovskite-type oxide exhibits a high oxygen mobility, which may contribute for the removal of carbon deposits [20]. However, carbon formation still happens during SR of toluene over Ni-based catalysts derived from perovskite- or hydrotalcite-type oxides.

The support can also play a key role in the SR of toluene by assisting in the removal of carbon or suppressing its formation. Redox supports such as ceria and ceria-containing mixed oxides improve catalyst stability due to their high oxygen storage capacity (OSC) and oxygen mobility. The OSC of cerium oxide is associated with its ability to reversibly change oxidation states between Ce^{4+}/Ce^{3+} by storing/releasing oxygen. This highly mobile oxygen can react with carbon species as soon as it forms, keeping the metal surface free of carbon and, thus inhibiting deactivation. Lamacz et al. [14] studied the SR of toluene over Ni or Co supported on $CeZrO_2$. TPD of toluene showed the formation of CO_2. Since there was no oxygen in the feed, toluene reacted only with oxygen from the support. However, long-term stability tests were not carried out.

Recent studies on SR of toluene have mainly been carried out using Ni-based catalysts in powder form, which are not suitable for industrial applications. Additionally, the monoliths can improve structural and thermal stability of catalytic reactors by (i) enhancing heat and mass transfer due to their high geometric surface area; (ii) reducing pressure drop, (iii) enabling fast response during transient operations, (iv) decreasing reactor weight and volume; and (v) avoiding reactor blocking [21]. For monolith-based reactors, precious metal are preferred over base metals oxides due to their high activity, allowing thin washcoats to be used, and thus achieving a better thermal and structural stability [22]. Besides not requiring to be activated during start up procedure and being highly resistant to coke formation, precious metals may also be recycled and reused.

To the best of our knowledge, only a few publications have studied the effect of noble metal supported catalysts on SR of toluene [23]. Wang and Gorte [23] investigated the performance of Pd/CeO_2, Pd/Al_2O_3 and Pt/CeO_2 catalysts for the SR of toluene using a water/toluene molar ratio of 2 at several reaction temperatures (623, 673, 723, and 773 K). Ceria supported catalysts were more active than Pd/Al_2O_3 catalyst. However, the authors did not evaluate the formation of carbon during the reaction.

Therefore, the aim of this work is to evaluate the performance of $Ce_xZr_{1-x}O_2/Al_2O_3$ supported Pt catalysts for SR of toluene and their stability toward deactivation by coke. Toluene was chosen as model molecule representative of tar. A better understanding of the catalyst physicochemical properties on activity and stability is expected to guide the rational design of new catalysts for tar removal from biomass gasification.

2 Experimental

2.1 Catalysts Preparation

The γ-Al_2O_3 (CATAPAL-A, Sasol) support was first calcined at 1173 K for 6 h using a heating rate of 10 K/min in a muffle. The alumina supported ceria and ceria–zirconia samples were prepared by co-impregnation of the alumina with an aqueous solution of cerium(IV) ammonium nitrate (99.99 %, Sigma-Aldrich) and zirconyl nitrate ($\sim$35 wt % solution in dilute nitric acid, >99 %, Sigma-Aldrich) as precursors of cerium and zirconium, respectively. First, the solution containing cerium(IV) ammonium nitrate and zirconyl nitrate was prepared, and then alumina was added. The solution was kept under stirring for 2 h. Later, the solvent was removed using a rotary evaporator and a silicon oil bath left at 343 K. The samples were dried at 383 K for 12 h and then calcined at 1073 K for 4 h in muffle at heating rate of 5 K/min. The $Ce_xZr_{1-x}O_2/Al_2O_3$ samples were prepared with 20 wt% of ceria or ceria–zirconia oxides, where $x = 0.5$, 0.75, and 1.0. The ceria or ceria-zirconia content was calculated in order to obtain a monolayer over the alumina surface, by taking into account the BET surface area of alumina and the crystallographic structure of the oxide [24]. Then, the catalysts were prepared by incipient wetness impregnation of the supports with an aqueous solution of chloroplatinic acid hydrate (H_2PtCl_6, 99.995 %, Sigma-Aldrich) in order to have 1.5 wt% of Pt. The catalysts were dried at 373 K in an air-circulating oven and calcined under air flow (50 mL/min) at 673 K for 2 h using a heating rate of 5 K/min.

2.2 Catalyst Characterization

The chemical composition of each sample was determined using a Rigaku RIX 3100 X-ray fluorescence spectrometer with a rhodium tube operated at 4 kW. The measurement technique applied was a semi-quantitative analysis. Calcined samples ($\sim$0.5 g) were analyzed as self-supported wafers.

The BET surface areas of the samples were measured using a Micromeritics ASAP 2020 analyzer by nitrogen adsorption at 77 K. Before the measurements, the samples (0.15–0.20 g) were dried at 373 K for 24 h and degassed at 623 K for 1 h.

The X-ray powder diffraction pattern of the calcined samples were obtained with CuK_α radiation ($\lambda = 1.5406$ Å) using a Rigaku Miniflex diffractometer. Data were collected under two different conditions: (i) over the 2θ range of 25° to 90° using a scan rate of 0.04°/step and a scan time of 1 s/step; (ii) 2θ from 27° to 32°, at a scan rate of 0.02°/step and counting times of 10 s/step. The Scherrer equation was used to estimate the crystallite mean diameter of CeO_2 particles.

The total acidity of the samples was determined by temperature-programmed desorption of ammonia (NH_3-TPD). Before the adsorption of ammonia, the samples were treated under air at 773 K (30 mL/min), for 1 h. The samples were cooled at 423 K in He flow (30 mL/min), and then treated with a mixture containing 20 vol% NH_3 in He (30 mL/min) for 30 min. The physisorbed ammonia was eliminated by flowing He (30 mL/min) for 1 h at 423 K. The NH_3-TPD was performed by heating the sample from 423 to 873 K at 20 K/min and monitoring the effluent gas composition by a mass spectrometer (Balzers, Omnistar).

Temperature-programmed reduction (TPR) measurements were performed in a Micromeritics AutoChem II 2920 Chemisorption Analyzer. Data acquisition and processing were performed using a AutoChem II version 3.05 software. Calcined samples (~0.45 g) were placed in a U-shaped quartz reactor and dried for 30 min in a flow of N_2 at 423 K. Then the samples were cooled down to room temperature. After that treatment, the catalysts were heated in a reducing gas mixture of 10 % vol H_2 in N_2 from room temperature until 1273 K at a heating rate of 10 K/min and flowrate of 30 mL/min.

The dehydrogenation of cyclohexane was used to determine the metal dispersion of $Ce_xZr_{1-x}O_2/Al_2O_3$ supported Pt catalysts. In this case, most commonly used techniques such as H_2 or CO chemisorption are not recommended for these catalysts due to the adsorption of both gases on ceria [25, 26]. Therefore, the Pt dispersion was determined by a correlation between the rate of cyclohexane dehydrogenation and platinum dispersion of a catalyst with known dispersion [27].

Cyclohexane dehydrogenation was performed in a fixed bed reactor at atmospheric pressure. The catalysts (10 mg) were first reduced at 773 K for 1 h and then they were heated up to 973 K (the temperature of steam reforming of toluene reaction) under He. The reaction was carried out at 543 K and WHSV = 120 h^{-1}. The reactants were fed into the reactor by bubbling H_2 through a saturator containing cyclohexane at 285 K (H_2/C_6H_{12} molar ratio of 13.6). At these conditions, no mass transfer or equilibrium limitations were observed. The conversions were kept below 10 %. The exit gases were analyzed using a gas chromatograph (Agilent 7890A) equipped with a HP-INNOWAX column.

Raman was used to characterize the nature of carbon formed on the catalysts after 24 h of time on stream (TOS). The Raman spectra were collected with a Horiba Jobin–Yvon LabRAM HR system equipped with a confocal microscope (Olympus EX-41), and a CCD (charge coupled device) detector. The excitation source was the 633 nm line of a He/Ne ion laser. The spectra of powder samples were taken at ambient conditions in the 1100–1800 cm^{-1} region. Spectra were processed with the LabSpec software version 5.58.25 provided by Horiba Jobin–Yvon.

2.3 Steam Reforming of Toluene

SR of toluene was performed in a U-shaped quartz reactor at atmospheric pressure and 973 K for 24 h. Prior to the reaction, the catalyst (20 mg) was reduced under H_2 at 773 K for 1 h, and maintained at this temperature for 30 min under He. Then the catalyst was heated up to the reaction temperature under He. The reactant mixture (0.5 % toluene; 20 % water; 79.5 % helium) was obtained by flowing two He streams (75 mL/min) through saturators containing toluene and water separately, and mixing them with a third He stream (150 mL/min). The exit gases were analyzed using a gas chromatograph (Agilent 6890) equipped with a thermal conductivity detector and Porapack Q and HP-INNOWAX columns. The toluene conversion and product distribution were determined from:

$$X_{toluene} = \frac{(n_{toluene})_{fed} - (n_{toluene})_{exit}}{(n_{toluene})_{fed}} \times 100 \quad (1)$$

$$Y_i = \frac{(n_i)_{produced}}{(n_{total})_{produced}} \times 100 \quad (2)$$

3 Results and Discussion

3.1 Catalyst Characterization

The metal content obtained by X-ray fluorescence for all catalysts is shown in Table 1. The Pt loading was close to the nominal value of 1.5 wt% Pt for all samples. The molar fractions of ceria were 0.72, 0.46 and 0.22 for the $Pt/Ce_xZr_{1-x}O_2/Al_2O_3$ catalysts with $x = 0.75$, 0.50, 0.25. Furthermore, traces of chlorine were not detected by XRF

Table 1 Chemical composition obtained by XRF and surface area for $Pt/Ce_xZr_{1-x}O_2/Al_2O_3$ catalysts

Sample	Pt (wt %)	CeO_2	ZrO_2	Al_2O_3	CeO_2 (mol%)	S_{BET} ($m^2\ g^{-1}$)
$Pt/CeO_2/Al_2O_3$	1.4	19.1	–	79.3	1.00	84
$Pt/Ce_{0.75}Zr_{0.25}O_2/Al_2O_3$	1.6	14.9	4.1	79.1	0.72	105
$Pt/Ce_{0.50}Zr_{0.50}O_2/Al_2O_3$	1.7	8.8	7.3	81.9	0.46	90
$Pt/Ce_{0.25}Zr_{0.75}O_2/Al_2O_3$	1.2	4.5	11.2	82.9	0.22	103

technique. The values of BET surface areas are also shown in Table 1. The addition of ceria or ceria-zirconia decreased the surface area of the calcined alumina (129 m^2/g).

The diffractograms of the supports are shown in Fig. 1A. All samples exhibited the lines corresponding to alumina phases (γ-alumina—PDF#10-0425; θ-alumina—PDF#11-0517; δ-alumina—PDF#46-1131). For CeO_2/Al_2O_3 sample, it is also noticed the lines characteristic of CeO_2 with cubic structure (CeO_2—PDF#34-0394). The addition of zirconia shifted these peaks to higher 2θ values due to changes in lattice parameter and formation of a ceria-zirconia solid solution with cubic symmetry [27–30]. The diffraction lines related to zirconia phases were not detected. The diffractograms of $Pt/Ce_xZr_{1-x}O_2/Al_2O_3$ catalysts (not shown here) were identical to the ones of the supports. The lines characteristic of platinum oxide were not detected likely due to the low metal loading of the samples.

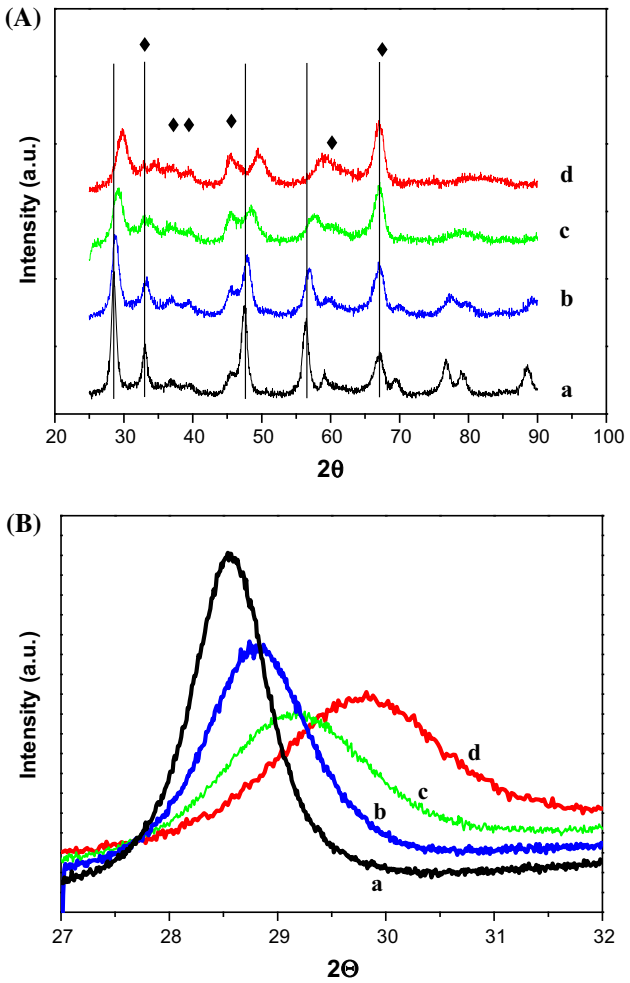

Fig. 1 X-ray diffraction patterns obtained for $Ce_xZr_{1-x}O_2/Al_2O_3$ supports between **A** $2\theta = 25°$ and 90° and **B** $2\theta = 27°$ and 32°. (*a*) CeO_2/Al_2O_3; (*b*) $Ce_{0.75}Zr_{0.25}O_2/Al_2O_3$; (*c*) $Ce_{0.5}Zr_{0.5}O_2/Al_2O_3$; and (*d*) $Ce_{0.25}Zr_{0.75}O_2/Al_2O_3$. *Diamond* alumina (γ-alumina—PDF#10-0425; θ-alumina—PDF#11-0517; δ-alumina—PDF#46-1131); CeO_2—PDF#34-0394

The phase composition of the ceria-zirconia solid solution can also be estimated by XRD using the 2θ position of the CeO_2 (111) reflection and a correlation reported by Kozlov et al. [31]. Therefore, diffractograms collected at slow scanning speed are presented in Fig. 1B and Table 2. The results showed that the lines corresponding to the reflection of CeO_2 (111) are symmetrical for all ceria-zirconia supported samples, indicating the formation of a homogeneous ceria-zirconia solid solution. The composition of the solid solution, which was calculated by the procedure proposed by Kozlov et al. [31], was: $Ce_{0.80}Zr_{0.20}O_2/Al_2O_3$, $Ce_{0.58}Zr_{0.42}O_2/Al_2O_3$ and $Ce_{0.20}Zr_{0.80}O_2/Al_2O_3$. Even though all samples exhibited solid solutions with compositions close to the expected nominal value, part of zirconia was not incorporated into ceria lattice.

The lines of ceria-zirconia supported samples were broader than the ones detected for CeO_2/Al_2O_3 sample. This is consistent with the crystallite sizes of CeO_2 determined by XRD analyses for $Ce_xZr_{1-x}O_2/Al_2O_3$ and $Pt/Ce_xZr_{1-x}O_2/Al_2O_3$ reported in Table 2. There is a clear decrease in crystallite size after addition of zirconium to

Table 2 Molar fraction of ceria and particle size determined by XRD for $Ce_xZr_{1-x}O_2/Al_2O_3$ and $Pt/Ce_xZr_{1-x}O_2/Al_2O_3$ catalysts

Sample	CeO_2 (mol%)	CeO_2 (nm)
$Pt/CeO_2/Al_2O_3$	0.88 (0.91)	9.4 (10.2)
$Pt/Ce_{0.75}Zr_{0.25}O_2/Al_2O_3$	0.77 (0.80)	6.3 (7.3)
$Pt/Ce_{0.50}Zr_{0.50}O_2/Al_2O_3$	0.60 (0.58)	5.2 (3.5)
$Pt/Ce_{0.25}Zr_{0.75}O_2/Al_2O_3$	0.26 (0.20)	5.7 (3.1)

Values in parenthesis denote the properties of the corresponding support (without Pt)

CeO_2 for both supports and catalysts. This result agrees very well with previous studies on ceria and ceria-zirconia-based catalysts using bulk and supported oxides [30]. The addition of Zr^{4+} to CeO_2 increases the thermal stability of the oxide, thus inhibiting the sintering process during calcination.

The total acidity of the samples was determined by NH_3-TPD and the results are reported in Table 3. The density of acid sites increased with an increase of zirconia content, changing from 3.36 μmol/m^2 ($Pt/CeO_2/Al_2O_3$) to 4.69 μmol/m^2 ($Pt/Ce_{0.25}Zr_{0.75}O_2/Al_2O_3$). The same result was obtained by Li and coworkers [32], who studied the acid properties of CeO_2-ZrO_2 mixed oxides containing different ceria content (0, 12, 50, 88, and 100 mol%) by using NH_3-TPD.

Figure 2A shows the TPR profiles for the $Ce_xZr_{1-x}O_2/Al_2O_3$ supports. The reduction profile of CeO_2/Al_2O_3 support (curve a) exhibited peaks around 673–873 K and above 873 K. The H_2 consumption at low temperature region is attributed to the removal of surface oxygen from ceria and to the formation of nonstoichiometric cerium oxides (CeO_x). The peak at high temperature range is assigned to the reduction of bulk ceria and the formation of Ce_2O_3 [33–35]. The TPR profile of $Ce_{0.75}Zr_{0.25}O_2/Al_2O_3$, $Ce_{0.50}Zr_{0.50}O_2/Al_2O_3$ and $Ce_{0.25}Zr_{0.75}O_2/Al_2O_3$ exhibited two peaks around 691–759 and 833–881 K and a small broad peak at higher temperature (1200 K). The addition of zirconia to ceria increased the hydrogen consumption at low temperature region whereas the hydrogen uptake at high temperature region decreased. Ceria reduction is favored by the addition of zirconium, leading to an increase of oxygen vacancies [30]. The largest mobility of oxygen increases the reducibility of the cerium–zirconium mixed oxide.

The reduction profiles of $Pt/Ce_xZr_{1-x}O_2/Al_2O_3$ catalysts are shown in Fig. 2B. All catalysts presented a well-defined peak at 460 K. A small and broad peak also appeared at 623 K in all profiles. The first peak at 460 K is attributed to the reduction of PtO_2 and the second is due to the reduction of superficial ceria promoted by the metal formed [26]. The peak around 1073–1173 K is attributed to bulk CeO_2 reduction [27, 28]. Increasing zirconia content significantly decreased the intensity of this high temperature peak,

Table 3 Total amount of NH_3 desorbed during TPD

Catalyst	Total amount of NH_3	
	($\mu mol/g_{cat}$)	($\mu mol/m^2$)
$Pt/CeO_2/Al_2O_3$	282.2	3.36
$Pt/Ce_{0.75}Zr_{0.25}O_2/Al_2O_3$	421.4	4.01
$Pt/Ce_{0.50}Zr_{0.50}O_2/Al_2O_3$	403.3	4.48
$Pt/Ce_{0.25}Zr_{0.75}O_2/Al_2O_3$	482.7	4.69

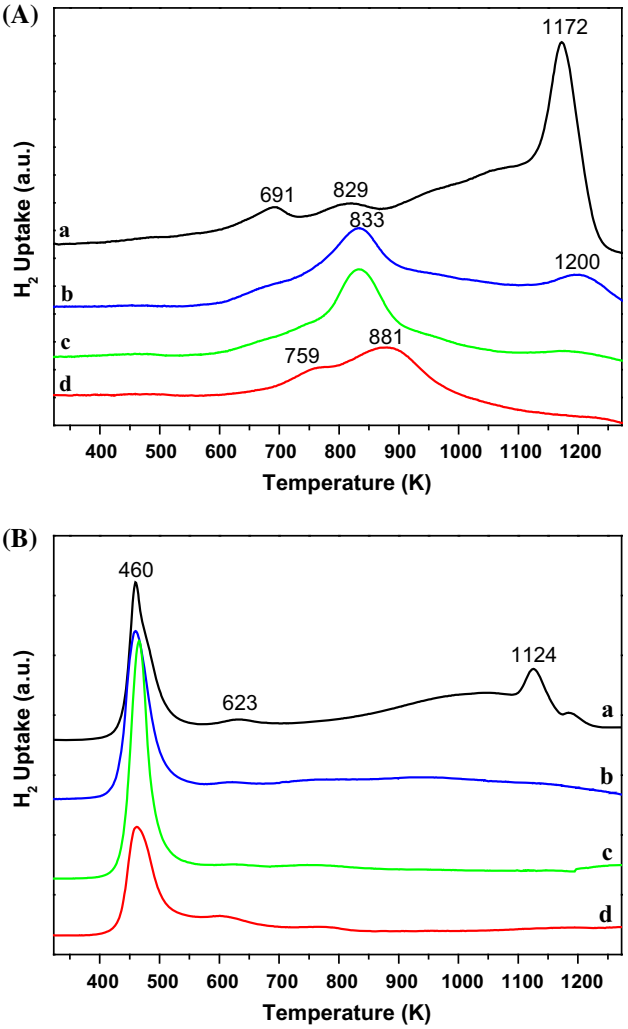

Fig. 2 **A** TPR profiles of supports: (*a*) CeO_2/Al_2O_3; (*b*) $Ce_{0.75}Zr_{0.25}O_2/Al_2O_3$; (*c*) $Ce_{0.5}Zr_{0.5}O_2/Al_2O_3$; and (*d*) $Ce_{0.25}Zr_{0.75}O_2/Al_2O_3$; **B** TPR profiles of catalysts: (*a*) $Pt/CeO_2/Al_2O_3$; (*b*) $Pt/Ce_{0.75}Zr_{0.25}O_2/Al_2O_3$; (*c*) $Pt/Ce_{0.5}Zr_{0.5}O_2/Al_2O_3$; and (*d*) $Pt/Ce_{0.25}Zr_{0.75}O_2/Al_2O_3$

which is no longer observed for $Ce_{0.25}Zr_{0.75}O_2/Al_2O_3$ catalyst.

The total hydrogen uptake on $Ce_xZr_{1-x}O_2/Al_2O_3$ and $Pt/Ce_xZr_{1-x}O_2/Al_2O_3$ is summarized in Table 4. The incorporation of Zr^{4+} into CeO_2 lattice significantly increased the hydrogen consumption and then its reducibility. The reducibility of the support is a very important issue related with its ability to generate oxygen vacancies and to transfer the oxygen onto the metal particle [36]. The promotional effect of Ce^{4+} on the oxygen transfer was shown by experiments of pulses of CH_4 and CO_2. A higher degree of reduction resulted in an increase in the number of oxygen vacancies formed near the metal particle and a subsequent increase in the ability to dissociate CO_2. In situ XPS studies revealed a correlation between the oxygen vacancies and the Ce/Zr ratio on $Pt/Ce_xZr_{1-x}O_2$ catalysts [37]. The reducibility of the support was enhanced when the mixed

Table 4 Hydrogen consumption obtained from TPR profiles of $Ce_xZr_{1-x}O_2/Al_2O_3$ and $Pt/Ce_xZr_{1-x}O_2/Al_2O_3$ catalysts

Sample	H_2 uptake ($\mu mol/g_{cat}$)	H_2 uptake ($\mu mol/g_{CeO2}$)
$Pt/CeO_2/Al_2O_3$	813 (613)	4261 (3213)
$Pt/Ce_{0.75}Zr_{0.25}O_2/Al_2O_3$	829 (421)	5559 (2823)
$Pt/Ce_{0.50}Zr_{0.50}O_2/Al_2O_3$	512 (329)	5845 (3756)
$Pt/Ce_{0.25}Zr_{0.75}O_2/Al_2O_3$	324 (283)	7165 (6258)

Values in parenthesis denote H_2 uptake of the corresponding support (without Pt)

solid is formed, and the percent of Ce^{3+} goes through a maximum for the catalyst with Ce/Zr ratio of 1.0. Fornasiero et al. [38] also reported that the reducibility of ceria-zirconia is strongly depended on the Ce/Zr ratio. Therefore, in our work, the enhancement of oxygen vacancies is due to the high oxygen mobility in the solid solution formed, which was corroborated by XRD data.

The platinum dispersion was determined using the dehydrogenation of cyclohexane as a model reaction. The reaction rates of dehydrogenation of cyclohexane and Pt dispersion for all catalysts are summarized in Table 5. The reaction rate values obtained were similar to the ones previously reported for supported Pt catalysts [24]. Increasing the zirconia content decreased the Pt dispersion. $Pt/Ce_{0.25}Zr_{0.75}O_2/Al_2O_3$ catalyst showed the lowest Pt dispersion (36 %), whereas the highest value was obtained for $Pt/CeO_2/Al_2O_3$ catalyst (83 %). These values are higher than the ones obtained in previous works [27, 28], and they are likely due to the higher alumina surface area of the present samples.

3.2 Steam Reforming of Toluene

The toluene conversion and product distribution as a function of TOS obtained for SR of toluene over $Pt/Ce_xZr_{1-x}O_2/Al_2O_3$ catalysts are shown in Fig. 3. $Pt/CeO_2/Al_2O_3$ catalyst exhibited the highest initial toluene conversion.

The reaction products were mostly H_2, CO_2 and CO. Low concentrations of benzene were measured at the beginning of reaction for $Pt/Ce_{0.50}Zr_{0.50}O_2/Al_2O_3$ and $Pt/Ce_{0.25}Zr_{0.75}O_2/Al_2O_3$ catalysts, and it was no longer detected after 200 min of TOS. It was not observed the formation of methane.

According to Duprez et al. [39], several reactions may occur during steam reforming of aromatic hydrocarbons such as: (i) dealkylation (C–C bond breaking in the side chains); (ii) dehydrogenation (on the side chain); and (iii) degradation (ring opening). The main reactions occurring during the steam reforming of toluene are listed below [8, 16]: Steam reforming of toluene

$$C_7H_8 + 7H_2O \rightarrow 11H_2 + 7CO \quad (3)$$

$$C_7H_8 + 14H_2O \rightarrow 18H_2 + 7CO_2 \quad (4)$$

Water–gas shift (WGS) reaction

$$CO + H_2O \rightarrow H_2 + CO_2 \quad (5)$$

Hydrodealkylation reaction

$$C_7H_8 + H_2 \rightarrow C_6H_6 + CH_4 \quad (6)$$

Steam reforming of methane

$$CH_4 + H_2O \rightarrow 3H_2 + CO \quad (7)$$

Duprez et al. [39] studied the SR of aromatic hydrocarbons at 713 K over supported Rh, Ni, and Pt catalysts. For SR of toluene, Rh and Ni led to the formation of dealkylation and ring-opening products. Pt was highly selective to dealkylation reaction, producing benzene. Wang and Gorte [23] studied the SR of toluene over Pd/CeO_2, Pd/Al_2O_3, and Pt/CeO_2 catalysts using a water/-toluene molar ratio of 2 and different reaction temperatures (623, 673, 723, and 773 K). Selectivities to benzene around 36–89 % were obtained for temperatures lower than 773 K. However, benzene was no longer observed at 773 K for the ceria supported catalysts. Similar results were observed in our high temperature tests (973 K).

In this study, the higher formation of CO_2 in comparison to CO is likely due to the promotion of WGS reaction on ceria-zirconia materials or the oxidation of CO by the oxygen from the support. The dealkylation of toluene to benzene and methane took place only at the beginning of the reaction. The methane formed either reacts

Table 5 Reaction rate and platinum dispersion obtained through cyclohexane dehydrogenation over $Pt/Ce_xZr_{1-x}O_2/Al_2O_3$ catalysts

Catalyst	Reaction rate [$mol/(g_{Pt}$ min)]	Pt dispersion (%)
$Pt/CeO_2/Al_2O_3$	0.294	83
$Pt/Ce_{0.75}Zr_{0.25}O_2/Al_2O_3$	0.246	69
$Pt/Ce_{0.50}Zr_{0.50}O_2/Al_2O_3$	0.232	65
$Pt/Ce_{0.25}Zr_{0.75}O_2/Al_2O_3$	0.127	36

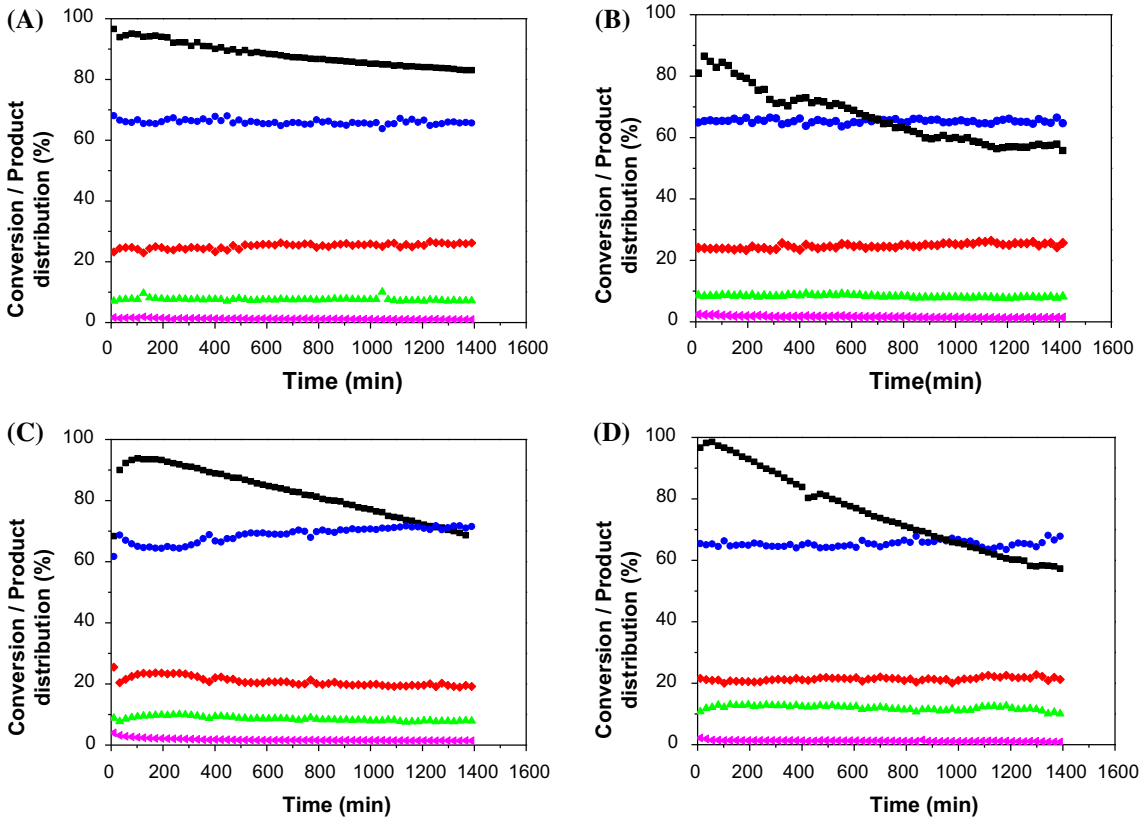

Fig. 3 Toluene conversion and product distribution as a function of TOS for SR of toluene over $Pt/Ce_xZr_{1-x}O_2/Al_2O_3$ catalysts. **A** $Pt/CeO_2/Al_2O_3$; **B** $Pt/Ce_{0.75}Zr_{0.25}O_2/Al_2O_3$; **C** $Pt/Ce_{0.5}Zr_{0.5}O_2/Al_2O_3$; and **D** $Pt/Ce_{0.25}Zr_{0.75}O_2/Al_2O_3$ Reaction conditions: $T_{reaction} = 973$ K; Q = 300 mL/min; H_2O/toluene molar ratio = 40; $m_{catal} = 20$ mg. *Black square* toluene conversion; selectivity to *blue circle* H_2; *green triangle* CO; *red diamond* CO_2; *pink triangle* Benzene

immediately with water producing H_2 and CO or may undergo further dehydrogenation to CH_x species and carbon. Therefore, the main reactions that take place over $Pt/Ce_xZr_{1-x}O_2/Al_2O_3$ catalysts are the SR of toluene and the WGS.

It was noticed that toluene conversion decreases over time mainly for all catalysts excepted for $Pt/CeO_2/Al_2O_3$ catalyst. This loss of activity has been attributed to the formation of carbon and it will be discussed in more detail in the following section.

3.3 Characterization of Post-reaction Catalysts

One of the main issues of the SR of toluene is catalyst deactivation by carbon deposition. Therefore, Raman spectroscopy was used to investigate the formation of carbon on spent catalysts after 24 h of TOS. This is a powerful tool for characterization of carbon materials since all allotropic forms of carbon such as carbon nanotubes, amorphous carbon, graphite, are active in Raman spectroscopy [40]. The position, linewidth, and relative intensity of bands depend on the carbon nature.

The Raman spectra of the used catalysts are shown in Fig. 4. It is noticed the presence of two bands in the range between 1200 and 1800 cm^{-1}, which are associated with

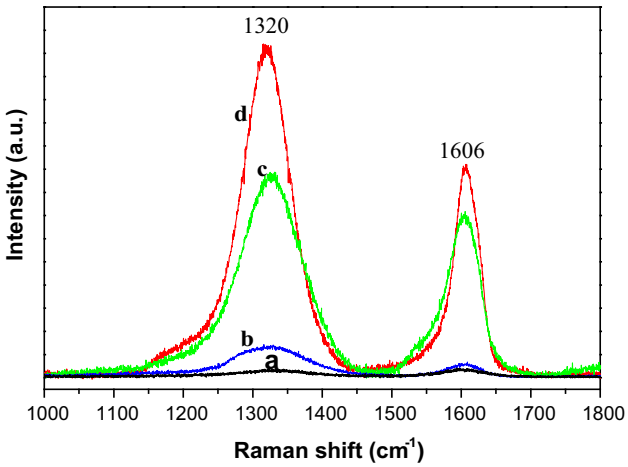

Fig. 4 Raman spectra of $Pt/Ce_xZr_{1-x}O_2/Al_2O_3$ catalysts after SR of toluene for 24 h (*a*) $Pt/CeO_2/Al_2O_3$; (*b*) $Pt/Ce_{0.75}Zr_{0.25}O_2/Al_2O_3$; (*c*) $Pt/Ce_{0.5}Zr_{0.5}O_2/Al_2O_3$; (*d*) $Pt/Ce_{0.25}Zr_{0.75}O_2/Al_2O_3$

the D and G vibration modes of carbon materials. The band at 1320 cm^{-1} (D mode) is attributed to disordered-induced Raman scattering from sp^2 carbons. The position and the linewidth of this band provide information about the nature of carbon [40]. For example, amorphous carbon exhibits a very broad linewidth (>100 cm^{-1}). The D bands in the range of 1285–1300 cm^{-1} with a linewidth of 10–30 cm^{-1} are characteristic of single-walled carbon nanotube (SWNT). Crystalline graphite-like forms and multi-walled carbon nanotubes (MWNT) show a D band at around 1305–1330 cm^{-1} and a width of about 30–60 cm^{-1}. The band at around 1606 cm^{-1}, the so-called G-mode, involves the in-plane bond-stretching motion of pairs of C sp^2 atoms [41]. For carbon nanotubes, this band splits into two peaks associated with the atomic displacements along circumferential (G−) and axial direction (G+) of the tube [42].

From the Raman spectra of Fig. 4, it is noticed that graphitic carbon was mainly formed on $Pt/Ce_xZr_{1-x}O_2/Al_2O_3$ catalysts during SR of toluene. The intensity of D and G bands varied depending on the catalyst. Increasing the zirconia content led to a significant increase in the intensities of these bands. The following order is observed for the intensities of these bands: $Pt/Ce_{0.25}Zr_{0.75}O_2/Al_2O_3 > Pt/Ce_{0.50}Zr_{0.50}O_2/Al_2O_3 \gg Pt/Ce_{0.75}Zr_{0.25}O_2/Al_2O_3$. However, carbon was not detected on $Pt/CeO_2/Al_2O_3$ catalyst. These results suggest that there is a relationship between the amount of carbon formed and the density of acid sites of the support as determined by NH_3-TPD. The higher amount of carbon was observed on the catalyst exhibiting the higher density of acid sites on the support (Table 3). In order to understand the remarkable resistance to carbon deposition on $Pt/CeO_2/Al_2O_3$ catalyst, the mechanism of carbon formation during this reaction will be discussed next.

3.4 General Discussion

The mechanism of coke formation over supported Ni catalysts during steam reforming of hydrocarbons is well described in the literature [19, 43–46]. High molecular weight hydrocarbons show a higher tendency for carbon formation on nickel than methane. The risk of carbon formation depends on the type of hydrocarbon, being higher for the aromatics compounds [44].

Significant carbon formation has been reported for the SR of toluene over different catalysts [4–7, 9, 11–13, 15, 16]. Therefore, a better understanding of reaction mechanism is necessary to rationally design a suitable catalyst for this reaction.

Toluene is initially adsorbed with its aromatic ring π bonded parallel to the metal surface [47]. Then, dealkylation of the methyl group of toluene takes place, leading to the formation of benzene and CH_x species [6]. The aromatic ring is hydrogenated to the saturated cyclic ring, which is broken, producing CH_x species on the surface of the catalyst. This CH_x species may be further dehydrogenated producing hydrogen and a highly reactive carbon species (C_α) [19]. This highly reactive carbon species may react with water from the feed to produce CO_x species. However, if the rate of hydrocarbon dissociation is faster than the rate of carbon oxidation, C_α formed may undergo polymerization to less active carbon (C_β). As a result, it may accumulate on the surface, either encapsulating the metal particle or dissolving into nickel lattice. The dissolution of carbon into the Ni crystallite is the first step for the nucleation and growth of carbon filaments (e.g., whiskers).

With respect to the noble metal-based catalysts, carbon formed can encapsulate the metal particles. In addition, noble metals generally have a lower tendency for carbon formation compared to nickel. It has been reported that the support plays an important role on the stability of supported noble metal catalysts on methane conversion reactions [48–50]. In the presence of a reducible oxide such as ceria and ceria-zirconia mixed oxides, carbon deposited on the surface of metallic particle reacts with oxygen from the support near to metal particle to produce CO and oxygen vacancies. Then, water from the feed may replenish the oxygen vacancies of the support, providing a redox mechanism for continuous cleaning. The balance between the rate of methane decomposition and the rate of cleaning determines the overall stability of the catalyst on the methane conversion reactions. Therefore, the stability of the catalyst is closely related to the OSC of the support. In our work, the addition of ZrO_2 increased the oxygen vacancies of the support as demonstrated by the total hydrogen uptake measured by TPR. The mobility of the oxygen from the support followed the order: $Pt/Ce_{0.25}Zr_{0.75}O_2/Al_2O_3 > Pt/Ce_{0.50}Zr_{0.50}O_2/Al_2O_3 > Pt/Ce_{0.75}Zr_{0.25}O_2/Al_2O_3 > Pt/CeO_2/Al_2O_3$. Therefore, it is expected that the catalyst containing the highest zirconia content shows the lowest carbon formation. However, the Raman spectra revealed the opposite tendency. These results indicate that the OSC of the support does not play a key role on the mechanism of carbon removal from the surface of the metallic particles. However, the tendency to carbon formation follows the Pt dispersion. Increasing Pt dispersion decreased the amount of carbon formed. This result is associated with the carbon formation mechanism. The CHx species produced by the decomposition of the aromatic ring can undergo further dissociation to C and H. According to Trimm [19], the dissociation of methane to give H and C requires a defined number of sites. Rostrup-Nielsen [18] proposed a critical ensemble size, below which carbon formation does not occur. Steam reforming requires ensembles of 3–4 atoms, whereas carbon formation needs

6–7 atoms. Therefore, the metal particle size significantly influences the nucleation rate of carbon. The initiation step for carbon formation is more difficult for smaller particle sizes, and this could explain the lower deposition of carbon on the catalyst with higher Pt dispersion.

Contrary to the SR of methane, where the molecule activation occurs only on the metal surface, toluene may also adsorbs on the support. Viinikainen et al. [51] studied the toluene adsorption over ZrO_2, Y_2O_3-ZrO_2 and SiO_2-ZrO_2 by diffuse reflectance infrared spectroscopy (DRIFTS) and TPD of toluene. Molecularly adsorbed toluene, benzoate species, and carbonaceous species were produced following the adsorption of toluene on these supports. Benzoate species were formed by the abstraction of hydrogen from the methyl group of toluene molecule and carbon bonding with two surface oxygen atoms of the support. This benzoate species may be decomposed to benzene and CO_2. In the presence of oxygen in the feed, the authors also reported the formation of benzyl species that were formed when one hydrogen atom from the methyl group was removed and toluene was adsorbed via the methylene group on the surface of the support. Toluene adsorption was also observed by infrared spectroscopy on $La_{0.7}Sr_{0.3}AlO_{3-\delta}$ (LSAO), and $LaAlO_3$ (LAO) perovskites used as supports for Ni catalysts [11]. According to the authors, high stability of the aromatic ring in toluene is achieved through the donation of electrons from π orbital to surface metal cations (La^{3+}, Sr^{2+} or Al^{3+}). Furthermore, the surface lattice oxygen strongly interacts with methyl group of toluene, and the formation of H–O bond also occurs. IR spectra identified bands attributed to the ν(OCO) stretching mode, indicating that adsorbed toluene was oxidized. However, the authors did not discuss the nature of this adsorbed species formed. The addition of water at 573 K promoted the decomposition of adsorbed species to CO and CO_2.

These works demonstrate that toluene also adsorbs on the support and may further react [11, 51]. In this case, hydrogen corresponding to the weakest C–H bond dissociation enthalpy is preferably removed from the methyl group, resulting in C_6H_6–CH_2^+ species [52]. Following this initial activation, alkylation of another toluene molecule with this intermediate on the acid sites of the support may result in the formation of methyl diphenyl and methyl triphenyl compounds [53]. These oligomers adsorbed on the surface will contribute to catalyst deactivation. A general scheme for carbon formation during SR of toluene over supported metallic catalysts is shown in Scheme 1.

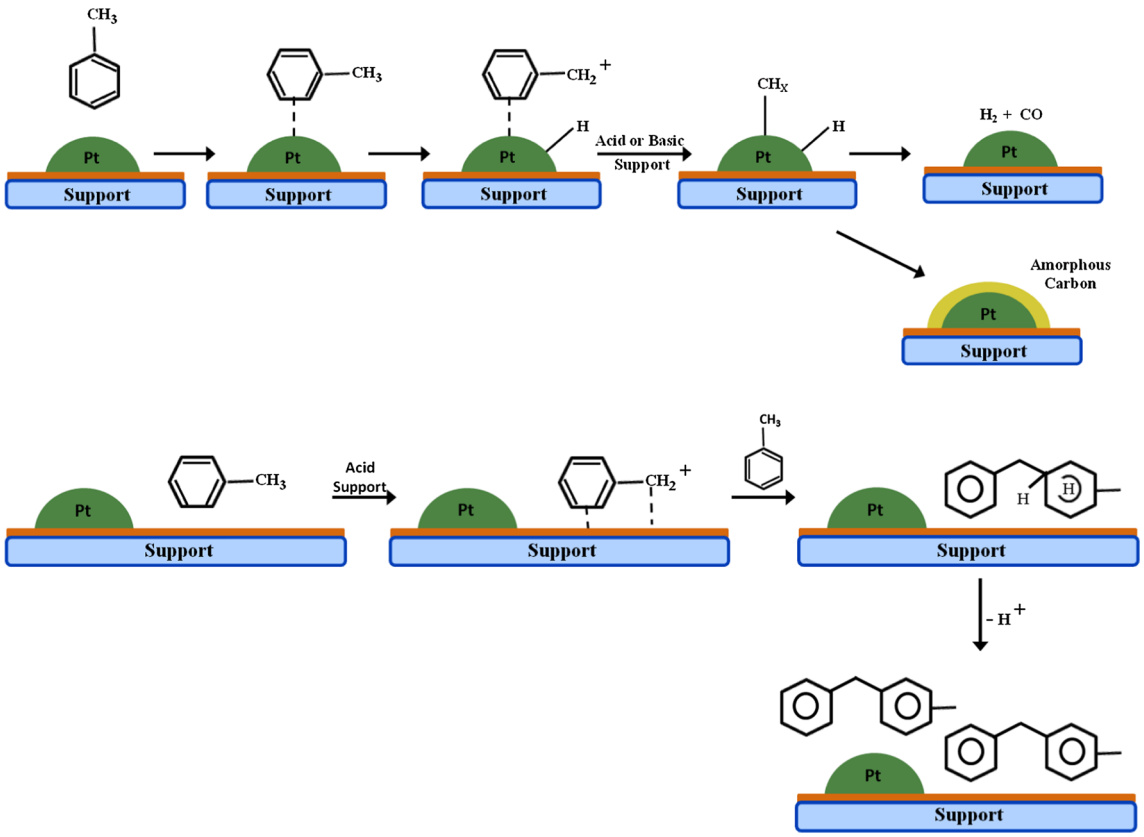

Scheme 1 Mechanism of carbon formation during SR of toluene over supported metallic catalysts

In this work, there is a clear correlation between the acidity of the catalyst and the amount of carbon formed over $Pt/Ce_xZr_{1-x}O_2/Al_2O_3$ catalysts. Decreasing the Ce/Zr ratio increased the density of acid sites as well as the amount of carbon formed. This result suggests that the main route for carbon deposition proceeds by the oligomerization of toluene molecule on the acid sites of the support. Since the mechanism of carbon removal by the oxygen from the ceria-zirconia solid solution takes place at the periphery of the metallic particles [48], the formation of carbon by oligomerization of toluene on the acid sites of the support may not be inhibited. In spite of the high OSC of $Ce_xZr_{1-x}O_2/Al_2O_3$ supports, carbon accumulates on the surface leading to catalyst deactivation. On the other hand, $Pt/CeO_2/Al_2O_3$ catalyst was quite stable during SR of toluene without carbon deposition. For this catalyst, ceria covered the acid sites of alumina and did not introduce significant Lewis acid sites. Moreover, ceria has also a high oxygen mobility that may contribute to the mechanism of carbon removal from the surface of the metallic particles. In addition, the effect of the Pt particle size on carbon deposition cannot be ruled out. Increasing Pt dispersion promoted catalyst stability. Therefore, all carbon formation routes are inhibited on $Pt/CeO_2/Al_2O_3$ catalyst that remains stable during reaction.

4 Conclusions

The addition of zirconia to ceria led to the formation of a homogeneous ceria-zirconia solid solution. Furthermore, increasing the zirconia content also increased the oxygen vacancies of the support as well as the density of acid sites from 3.36 μmol/m^2 ($Pt/CeO_2/Al_2O_3$) to 4.69 μmol/m^2 ($Pt/Ce_{0.25}Zr_{0.75}O_2/Al_2O_3$). The formation of oxygen vacancies is favored by the high oxygen mobility in the solid solution formed.

All catalysts deactivate during SR of toluene, except for $Pt/CeO_2/Al_2O_3$ catalyst. Raman spectroscopy revealed the formation of carbon on $Pt/Ce_xZr_{1-x}O_2/Al_2O_3$ catalysts. Increasing the zirconia content led to a significant increase in the intensities of the Raman bands corresponding to carbon materials. The following order was observed for the intensities of these bands: $Pt/Ce_{0.25}Zr_{0.75}O_2/Al_2O_3 > Pt/Ce_{0.50}Zr_{0.50}O_2/Al_2O_3 \gg Pt/Ce_{0.75}Zr_{0.25}O_2/Al_2O_3$. However, carbon was not detected on $Pt/CeO_2/Al_2O_3$ catalyst. The higher amount of carbon formed was observed on the catalyst exhibiting the higher density of acid sites on the support. This result suggests that the main route for carbon deposition proceeds by the oligomerization of toluene molecule on the acid sites of the support. A reaction mechanism for carbon formation during SR of toluene over support metallic catalysts was proposed. In this mechanism, hydrogen from the methyl group is abstracted, resulting in $C_6H_6–CH_2^+$ species. Following this initial activation, alkylation of another toluene molecule with this intermediate on the acid sites of the support may result in the formation of methyl diphenyl and methyl triphenyl compounds. These oligomers adsorbed on the surface will contribute to catalyst deactivation. However, Pt particle size also plays an important role on carbon deposition. Decreasing Pt particle size inhibited the deposition of carbon. $Pt/CeO_2/Al_2O_3$ catalyst was quite stable during SR of toluene without carbon deposition. For this catalyst, ceria covered the acid sites of alumina and did not introduce significant Lewis acid sites.

Acknowledgements The authors acknowledge the scholarship received from Research Support Foundation of Rio de Janeiro (FAPERJ). The authors are also grateful for support from The National Council for Scientific and Technological Development—CNPq (407144/2013-7). We also thank Marcos Anacleto and COPPE/UFRJ for the NH_3-TPD experiments.

References

1. Tung MM, Jablonski WS, Magrini-Bair KA (2009) Energy Fuels 23:1874
2. Abu El Rub Z, Bramer EA, Brem G (2004) Ind Eng Chem Res 43:6911
3. Coll R, Salvadó J, Farriol X, Montané D (2001) Fuel Process Technol 74:19
4. Srinakruang J, Sato K, Vitidsant T, Fujimoto K (2005) Fuel 85:2419
5. Zhang R, Wang Y, Brown RRC (2007) Energy Convers Manag 48:68
6. Swierczynski D, Libs S, Courson C, Kiennemann A (2007) Appl Catal B 74:211
7. Virginie M, Courson C, Niznamsky D, Chaoui N, Kiennemann A (2010) Appl Catal B 101:90
8. Bona S, Guillén P, Alcalde JG, García L, Bilbao R (2008) Chem Eng J 137:587
9. Ashok J, Kawi S (2013) Int J Hydrogen Energy 38:13938
10. Zhang, Hongwei C, Xionggang L, Weizhong D, Guozh Z (2009) Rare Metals 28:582
11. Mukai D, Murai Y, Higo T, Tochiya S, Hashimoto T, Sugiura Y, Sekine Y (2013) Appl Catal A 466:190
12. Sekine Y, Mukai D, Murai Y, Tochiya S, Izutsu Y, Seriguchi K, Hosomura N, Arai H, Kikuchi E, Sugiura Y (2013) Appl Catal A 451:160
13. Soongprasit K, Aht-Ong D, Sricharoeenchaikul V, Atong D (2012) Curr Appl Phys 12:580
14. Lamarcz A, Krzton A (2009) Catal Lett 128:40
15. Oemar U, Ang ML, Hee WF, Hidajat K, Kawi S (2014) Appl Catal B 148:231
16. Oemar U, Ang PS, Hidajat K, Kawi S (2013) Int J Hydrogen Energy 38:5525
17. Li C, Hirabayashi D, Suzuki K (2009) Fuel Proc Technol 90:790
18. Rostrup-Nielsen JR (1984) J Catal 85:31
19. Trimm DL (1997) Catal Today 37:233
20. Pena MA, Fierro JLG (2001) Chem Rev 101:1981
21. Tomasic V (2007) Catal Today 119:106
22. Farrauto RJ (2014) Chem Eng J 238:172
23. Wang X, Gorte RJ (2002) Appl Catal A 224:209

24. Silva FA, Martinez DS, Ruiz JAC, Mattos LV, Hori CE, Noronha FB (2008) Appl Catal A 335:145
25. Rogemond E, Essayem N, Frety R, Perrichon V, Primet M, Mathis F (1997) J Catal 166:229
26. Pantu P, Gavalas G (2002) Appl Catal A 223:253
27. Silva PP, Silva FA, Portela LS, Mattos LV, Noronha FB, Hori CE (2005) Catal Today 107:734
28. Silva PP, Silva FA, Souza HP, Lobo AG, Mattos LV, Noronha FB, Hori CE (2005) Catal Today 101:31
29. Hori CE, Permana H, KY Simon Ng, Brenner A, More K, Rahmoeller KM, Belton D (1998) Appl Catal B 16:105
30. Farias EC, Neto RCR, Colman RC, Noronha FB (2014) Catal Today 228:138
31. Kozlov AI, Kim DH, Yezerets A, Andersen P, Kung HH, Kung MC (2002) J Catal 209:417
32. Li Y, He D, Zhu Q, Zhang X, Xu B (2004) J Catal 221:584
33. Yao HC, Yao YF (1984) J Catal 86:254
34. Shyu JZ, Otto K (1989) J Catal 115:16
35. Santos ACSF, Damyanova S, Teixeira GNR, Mattos LV, Noronha FB, Passos FB, Bueno JMC (2005) Appl Catal A 290:123
36. Stagg-Williams SM, Noronha FB, Fendley G, Resasco DE (2000) J Catal 194:240
37. Noronha FB, Fendley EC, Soares RR, Alvarez WE, Resasco DE (2001) Chem Eng J 82:21
38. Fornasiero P, Di Monte R, Ranga Rao G, Kaspar J, Meriani S, Trovarelli A, Graziani M (1995) J Catal 151:168
39. Duprez D, Miloudi A, Delahay G, Maurel R (1986) J Catal 101:56
40. Belin T, Epron F (2005) Mater Sci Eng B 119:105
41. Ferrari AC, Robertson J (2000) Phys Rev B 61:14095
42. Dresselhaus MS, Dresselhaus G, Hofmann M (2007) Vib Spectrosc 45:71
43. Rostrup-Nielsen JR (1993) Catal Today 18:305
44. Rostrup-Nielsen JR, Rostrup-Nielsen T (2002) CATTECH 6:150
45. Rostrup-Nielsen JR, Sehested J, Norskov (2002) J Adv Catal 47:65
46. Trimm DL (1999) Catal Today 49:3
47. Coats AM, Cooper E, Raval R (1994) Surf Sci 307–309:89
48. Mattos LV, Rodino E, Resasco DE, Passos FB, Noronha FB (2003) Fuel Process Technol 83(147):161
49. Noronha FB, Shamsi A, Taylor C, Fendley EC, Stagg-William S, Resasco DE (2003) Catal Lett 90:13
50. Ruiz JAC, Passos FB, Bueno JMC, Souza-Aguiar EF, Mattos LV, Noronha FB (2008) Appl Catal A 334:259
51. Viinikainen T (2013) Appl Catal B 142:769
52. O'Malley A, Hodnett BK (1999) Catal Today 54:31
53. Guisnet M, Ribeiro FR (2004) Zeólitos, um nanomundo ao serviço da catálise, Fundação Calouste Gulbenkian